Microporous and Mesoporous Materials 299 (2020) 110118

Contents lists available at ScienceDirect

Microporous and Mesoporous Materials

journal homepage: http://www.elsevier.com/locate/micromeso

On mechanism of formation of SBA-15/furfuryl alcohol-derived mesoporous carbon replicas and its relationship with catalytic activity in oxidative dehydrogenation of ethylbenzene

Paula Janus [a], Rafał Janus [b,c,*], Barbara Dudek [a], Marek Drozdek [a], Ana Silvestre-Albero [d], Francisco Rodríguez-Reinoso [d], Piotr Kuśtrowski [a]

[a] Jagiellonian University, Faculty of Chemistry, ul. Gronostajowa 2, 30-387, Kraków, Poland
[b] AGH University of Science and Technology, Faculty of Energy and Fuels, al. A. Mickiewicza 30, 30-059, Krakow, Poland
[c] AGH University of Science and Technology, AGH Centre of Energy, ul. Czarnowiejska 36, 30-054, Krakow, Poland
[d] Universidad de Alicante, Departamento de Química Inorgánica, Apartado 99, E-03080, Alicante, Spain

ARTICLE INFO

Keywords:
CMK-3
CMK-5
Nanocasting
Oxidative dehydrogenation of ethylbenzene
Styrene

ABSTRACT

A series of CMK-3-like carbon replicas was synthesized by precipitation polycondensation of furfuryl alcohol in an aqueous slurry of SBA-15 at a polymer/SiO_2 mass ratio of 0.50–2.00. Changes in textural and structural parameters of SBA-15 after polymer deposition were studied by N_2 adsorption and X-ray diffraction. Morphology of the replicas was investigated by transmission electron microscopy, while their surface composition was determined by temperature-programmed desorption and X-ray photoelectron spectroscopy. The mechanism of deposition of poly(furfuryl alcohol) (PFA) onto silica surface was elucidated. It was found that PFA accumulates in SBA-15 pores randomly; certain channels are completely filled, while others remain partially empty. The incomplete filling of mesopores results in "*pseudo*-CMK-3" structures featuring the bimodal porosity (the typical mesopores of CMK-3 are accompanied by broader ones formed by the coalescence of adjacent partially hollow pores). The total filling of pores with PFA leads to the formation of good-quality CMK-3. The carbon replicas exhibited the presence of abundant amounts of superficial oxygen-containing moieties. These entities are responsible for high activity of the materials in the oxidative dehydrogenation (ODH) of ethylbenzene, bringing evidence supporting the mechanism of *active coke*, considered as governing the catalytic performance of carbon materials in ODH of alkanes.

1. Introduction

Over the recent two decades, ordered mesoporous carbon materials (OMCs) have been extensively studied by many researchers due to their unusual, beneficial properties, which surpass the features of conventional microporous activated carbons (AC). The highly ordered, adjustable porous structure of OMCs, exhibiting negligible diffusion limitations and the surface properties similar to AC, open up the opportunity to use them in plenty of applications. Indeed, nowadays, the OMC materials are omnipresent in almost all the chemistry-related scientific fields, including catalysis, adsorption, electrochemistry, solar technology, medicine, pharmacy, and microbiology [1–6]. Among the OMCs, the family of CMK-n carbon replicas reported for the first time in 1999 and further developed by the researchers from KAIST, is of a special interest [7,8]. The CMK-n materials are synthesized by the nanocasting strategy, which involves the use of an ordered porous matrix (usually silica) serving as the structure-directing agent (so-called *hard template*). After filling the pore system of the matrix with a carbon precursor (i.e. sucrose, aromatic hydrocarbons, polymers), followed by carbonization and etching of the mineral matrix, the resulting carbon framework shows the negative (inverse) structure of the applied silica. Therefore, morphology, structure, and textural characteristic of the ultimate replica are governed by the geometry and size of channels in the starting SiO_2 template, as well as a level of its pore filling with a carbon precursor and homogeneity of the incorporated polymer material. Generally, when it comes to accumulation of the polymer, two scenarios are possible. In the first case, a carbon precursor cladding an inner surface of silica matrix forms a homogeneous film. As a consequence, the

* Corresponding author. AGH University of Science and Technology, Faculty of Energy and Fuels, al. A. Mickiewicza 30, 30-059, Krakow, Poland.
E-mail address: rjanus@agh.edu.pl (R. Janus).

https://doi.org/10.1016/j.micromeso.2020.110118
Received 27 January 2020; Accepted 19 February 2020
Available online 22 February 2020

ultimate replica is constituted of hollow carbon nanopipes merged by thinner carbon bridges. Such structure cast from SBA-15 is known as the CMK-5 material. The second variant involves a complete filling of silica mesopores resulting in a formation of bulky carbon *nanorods* in the ultimate replica. In this case, the CMK-3 framework is formed [9].

Both CMK-3 and CMK-5 replicas, synthesized by nanoreplication of the *honeycomb* pore structure of SBA-15 mesoporous silica with the p6mm space group, show the same 2D hexagonal array of carbon *nanorods* or *nanopipes*, respectively. The entire framework of the replica is merged by the carbon bridges formed in narrower meso- and micropores present in the silica matrix [10]. The more often studied CMK-3 replica is typically characterized by BET specific surface area of 1000–1500 m^2/g, homogeneous pore system, uniform in a size of ca. 3.0–3.5 nm, and total pore volume of ca. 1.0–1.5 cm^3/g [10–12]. As the more subtle, the openwork structure of CMK-5 is built of the carbon *nanopipes*, in which the primary mesopores between the adjacent tubes are accompanied by the additional fraction of the mesopores (usually larger) present inside these tubes [13]. The CMK-5 materials exhibit a higher surface area (>2000 m^2/g) and total pore volume (up to ca. 2.5 cm^3/g) compared to the analogous CMK-3 carbons [14,15]. Such textural parameters make CMK-5 excellent host material for supporting of nanoparticles in a variety of advanced functional materials [16,17].

The overall procedure used for the synthesis of both CMK-3 or CMK-5 replicas relies on four essential steps: (i) preparation of a SBA-15 silica template, (ii) deposition of a carbon precursor in the pore structure of SBA-15, (iii) carbonization of the polymer/silica composite, and (iv) removal of the silica matrix [18]. The structure of resulting materials may be precisely tailored by a careful adjustment of synthesis conditions. There is a variety of synthesis procedures reported in the literature. However, a majority of differences in these strategies refer to the step of carbon precursor deposition. The pioneering synthesis of CMK-3 material reported by Jun et al. [10] involved incipient wetness impregnation of SBA-15 template with an acidified solution of sucrose, followed by an acid-catalyzed polymerization of sugar, subsequent carbonization at 900 °C, and etching of silica with a HF or NaOH solution. Fuertes et al. [9,19,20] reported the synthesis of CMK-3 replica by incipient wetness impregnation or, alternatively, chemical vapor deposition (CVD) of furfuryl alcohol (FA) as the carbon precursor into the pore system of SBA-15 impregnated initially with *p*-toluenesulfonic acid (a polymerization catalyst). Using acetonitrile and styrene as the carbon precursors in the CVD method was tested by Xia et al. [21–23]. It was shown that this procedure enabled to control precisely morphology, pore size, and degree of graphitization of the resulting carbons [21,24]. Another method reported in the synthesis of CMK-3 carbon replica consists in chemical interaction of a carbon precursor with intrinsic surface entities of siliceous matrix. This approach was developed by Yokoi et al. [25], whom described accumulation of FA based on its esterification with superficial SBA-15 silanol groups (i.e. chemical anchoring of polymer chains by a formation of polymer-silica covalent bonds).

In order to synthesize CMK-5 successfully, several pivotal parameters have to be appropriately adjusted: (i) porosity and surface composition of a silica matrix, (ii) selection of a suitable type of carbon precursor and its amount used, (iii) strategy of homogeneous incorporation of carbon precursor into silica mesochannels, (iv) temperature and duration of the synthesis, (v) type of a catalyst of polyreaction and method of its introduction, and (vi) carbonization conditions (heating rate, temperature, time, and kind of atmosphere) [9,26–31]. Interestingly, the carbonization under vacuum [28] and the use of a non-polar solvent during the FA polycondensation [29] were recognized as additional factors determining (or facilitating) the successful formation of CMK-5 framework. Joo et al. [26] synthesized originally the CMK-5 carbon replica by the introduction of FA into Al-containing SBA-15 (Si/Al molar ratio of 20) using the incipient wetness technique. In this approach, the wall-incorporated Al^{3+} centres served as Lewis acid sites catalyzing FA polycondensation.

In our previous paper [18], we reported a new facile method of synthesis of CMK-3 carbon replica based on Brønsted acid-catalyzed precipitation polycondensation of FA in the pore system of SBA-15. The synthesis was carried out in a FA-containing water slurry of the silica matrix in the presence of hydrochloric acid. Thus, it was proven that the deposition of the carbon precursor takes place regardless of whether the catalyst is immobilized onto the surface of the silica walls or not. The promising results inspired us to deepen the study on the mechanism of formation of polymeric films/rods inside the SBA-15 pores with an increasing carbon precursor content. Herein, we describe the synthesis of a series of CMK-like materials using SBA-15 with mesopores size (ca. 8 nm) wider than typically at different PFA/SBA-15 mass ratios. Such approach allowed us to investigate in details the evolution of textural and structural features of the carbon/-silica composites and the corresponding carbon replicas. Finally, chosen carbon replicas were tested as catalysts in the oxidative dehydrogenation of ethylbenzene. It was found that the promising catalytic performance of the studied materials surpassing the formerly studied activated carbons and carbon nanotubes, arises from their favorable surface chemistry, namely the presence of phenolic and carbonyl/quinone moieties. These beneficial entities are formed when the freshly carbonized PFA/SBA-15 composite comes into contact with air.

2. Experimental section

2.1. Synthesis

All reagents and solvents were commercially available and used without further purification: poly(ethylene oxide)-*block*-poly(propylene oxide)-*block*-poly(ethylene oxide) copolymer (Pluronic P123, $EO_{20}PO_{70}EO_{20}$, Sigma-Aldrich), tetraethyl orthosilicate (TEOS, 99.0%, Sigma-Aldrich), furfuryl alcohol (FA, 98%, Sigma-Aldrich), hydrochloric acid (HCl, 33%, Avantor Performance Materials Poland), hydrofluoric acid (HF, 40%, Avantor Performance Materials Poland), and ethylbenzene (EB, 99.8%, Sigma-Aldrich).

2.1.1. SBA-15

Mesoporous SBA-15 silica was synthesized at a molar gel composition of 1.00 TEOS: 0.02 Pluronic P123: 2.94 HCl: 116.46 H_2O, according to the procedure adapted from the paper by Michorczyk et al. [32]. In order to obtain a material with larger pores, this procedure was slightly modified. Namely, after TEOS hydrolysis, the obtained precipitate was subjected to the aging process at higher temperature (100 °C) and for prolonged time (72 h) when compared to the typical procedure (15–24 h at 80–90 °C) (details described in Supplementary Information) [18,32–34]. Furthermore, a small portion of the as-made material (ca. 0.40 g) was subjected to calcination using the same temperature regime as during the thermal treatment of the PFA/SBA-15 composites, as described later on (850 °C for 4 h at a heating rate of 1 °C/min, nitrogen atmosphere, 40 cm^3/min). This sample was marked as SBA-15_850.

2.1.2. Carbon replicas

A series of carbon replicas was synthesized by the acid-catalyzed precipitation polycondensation of various amounts of FA in an aqueous slurry of the silica template, according to the procedure described in our former paper [18]. Briefly, an amount of 3.00 g of freshly calcined SBA-15 was added under stirring to a mixture of FA and distilled water in a three-neck round-bottom flask (250 cm^3) placed in an oil bath on a magnetic stirrer and equipped with a reflux condenser. The intended mass ratio of FA/silica ranging within 0.50–2.00 (namely 0.50, 1.00, 1.25, 1.50, and 2.00) was adjusted by the amount of monomer used. The total mass of distilled water together with monomer was kept constant at 100.00 g for each synthesis batch. The mixture of SBA-15 immersed in FA + H_2O was agitated at room temperature for 30 min, and then HCl was introduced dropwise at the HCl/FA molar ratio of 6.0. After the mixture was heated to 100 °C, the reaction system was

isothermally held for next 6 h under vigorous stirring (400 rpm). The resulting brown solid, being the composite of poly(furfuryl alcohol) (PFA) and SBA-15 (PFA/SBA-15), was then isolated, washed with distilled water and dried at room temperature overnight. The as-synthesized composites were marked as PFA/S-*x*, where *x* suffix means the intended PFA/SBA-15 mass ratios. The PFA/S-*x* composites were carbonized in a tubular furnace under a N_2 atmosphere (40 cm^3/min) at 850 °C for 4 h at a heating rate of 1 °C/min. Finally, the silica template was removed by etching with 5 wt% HF solution at room temperature for 90 min (30.0 cm^3 of HF solution was used per 1.00 g of a solid). The procedure was repeated twice. The carbonized PFA/SBA-15 composites and corresponding replicas were labelled as C/S-*x* and C-*x*, respectively.

2.2. Characterization methods

Textural parameters of the materials were determined by means of low-temperature adsorption-desorption of nitrogen (−196 °C). The isotherms were collected using an ASAP 2020 instrument (Micromeritics). Prior to the analyses, the samples were outgassed at 350 °C for 5 h under vacuum. The Brunauer–Emmett–Teller model was used to calculate specific surface areas (S_{BET}) (within p/p_0 = 0.05–0.20). The external surface ($S_{ext.}$) was computed based on the slopes of linear functions fitted to α_s plots in the range of α_s = 1.70–2.50. The micropore surface (S_{micro}) was assessed based on the *t*-plot model (de Boer equation at p/p_0 = 0.05–0.20). Two models, namely non-local density functional theory (NLDFT; adsorption branch of isotherm, cylindrical pore symmetry assumption), and quenched solid density functional theory (QSDFT; equilibrium model, slit pore geometry), were employed for calculation of pore size distributions (PSDs) (the first one for the pristine silicas, and PFA/SBA-15 carbonizates, while the latter one for the carbon replicas). The total pore volumes (V_{total}) were extracted from the adsorption branches of the isotherms based on the respective data points at p/p_0 = 0.97–0.98 (single-point algorithm; s-p). The micropore volumes (V_{micro}) were calculated by the α_s-plot method within the range of α_s = 0.50–0.80. For this purpose, the reference macroporous silica LiChrospher (for pure silicas and carbonizates) [35], and non-porous carbon LMA10 [36] (for final replicas) were used. In the case of the replicas with the bimodal mesoporosity, the primary and secondary mesopore volumes ($V_{meso\ I}$, and $V_{meso\ II}$, respectively) were computed based on Lorentz deconvolution of QSDFT pore size distribution profiles.

A wall thickness of pure silicas ($w_{sil.}$) was calculated by subtracting a respective a_{100} lattice parameter (determined by XRD) and mean mesopore NLDFT diameter (D) (Supplementary Information, Eq. (S1)). The diameters of carbon nanorods in the replicas ($w_{carb.}$) were assessed by the simple geometrical model proposed by Joo et al. [37], while the respective mesopore widths (D) were additionally estimated (for the comparative purposes with QSDFT) from the expression reported by the same authors (cf. Supplementary Information, Eqs. (S2–S3)).

Replication fidelity index (RFI) for the carbon replicas was calculated based on respective textural parameters in the same manner as reported in our recent paper [38], with regard to the silica matrix calcined at 850 °C as a reference (cf. Supplementary Information, Eq. (S4)).

Structural parameters of the studied samples were examined by low-angle X-ray powder diffraction (XRD) using a Bruker D2 Phaser instrument equipped with a LYNXEYE detector. The diffraction patterns were collected with Cu Kα radiation (λ = 1.54184 Å) in a 2θ range of 0.80–3.15° with a step of 0.02°.

Thermogravimetric measurements (TG) were performed using a SDT Q600 instrument (TA Instruments). An amount of ca. 10 mg of a sample placed in a corundum crucible was heated from 30 °C to 1000 °C at a heating rate of 20 °C/min in an air atmosphere (100 cm^3/min). Real PFA/SBA-15 mass ratios were determined by dividing the mass loss within the range of 130–1000 °C, i.e. organic part of composite, by the mass recorded at 1000 °C, i.e. mineral part, while pore filling degrees were computed as a ratio of volume of bulky PFA deposited in 1.00 g of SiO_2 with regard to single-point total pore volumes of the SBA-15 matrix, assuming the density of bulky PFA equal to 1.55 g/cm^3 [38]. The same TG equipment was used to perform the experiment simulating the process of carbonization with subsequent air exposure, followed by temperature-programmed desorption under the respective atmospheres (nitrogen or air; both at a flow rate of 100 cm^3/min).

Transmission electron microscopy (TEM) images were taken with a JEOL microscope (model JEM-2010) equipped with an INCA Energy TEM 100 analytical system and a SIS MegaView II camera, working at the accelerating voltage of 200 kV. Prior to the imaging, samples were suspended in ethanol and placed on copper grids with a carbon film support (LACEY).

Temperature-programmed desorption (TPD) experiments were carried out using an U-shaped quartz reactor coupled directly to a quadrupole mass spectrometer (Balzer MSC 200). An amount of 100 mg of a sample was heated from 20 °C to 1000 °C at a heating rate of 10 °C/min under a helium flow (50 cm^3/min; grade 5.0). The quantities of evolved CO and CO_2 were calculated after calibration based on calcium oxalate decomposition [39]. The TPD profiles were deconvoluted according to the Gauss formalism.

X-ray photoelectron spectroscopy (XPS) measurements were performed with a Prevac photoelectron spectrometer equipped with a hemispherical analyzer VG SCIENTA R3000. The spectra were recorded using a monochromatized aluminum source Al Kα (E = 1486.6 eV). The base pressure in the analytical chamber was $5{\cdot}10^{-9}$ mbar. The binding energy scale was calibrated using the Au $4f_{7/2}$ line of a cleaned gold sample at 84.0 eV. The surface composition of carbon materials was studied based on the areas and binding energies of C 1*s* and O 1*s* core levels. The spectra were fitted using the CasaXPS software (Casa Software Ltd.).

2.3. Catalytic tests

Carbon replicas were tested as catalysts in the oxidative dehydrogenation (ODH) of ethylbenzene (EB) to styrene in the presence of oxygen as an oxidizing agent. The catalytic runs were carried out in a flow-type tubular quartz microreactor (internal diameter of 8 mm) placed in a vertically-oriented electric tunnel furnace and filled with 50 mg of a catalyst held up by a quartz wool plug. A constant flow of gaseous reactants was controlled by mass flow controllers (Brooks 4800 Series). The total flow of He + O_2 mixture was equal to 3.000 dm^3/h (0.024 dm^3/h of O_2 of grade 5.0 diluted in the stream of 2.976 dm^3/h of helium of grade 5.0). The influent gas mixture was saturated with EB vapor by bubbling through a glass saturator filled with liquid EB, kept at 25 °C. The molar ratio of O_2: EB was kept constant at 1:1. Reaction products were analyzed in a Bruker 450-GC gas chromatograph equipped with three packed columns (Porapak Q, Molecular Sieve 4A, and Chromosorb W-HP), and three detectors (two flame ionization detectors; one among them equipped with a methanizer enabling CO_x quantification, and one thermal conductivity detector). Prior to a catalytic run, a catalyst was evacuated at 200 °C for 30 min in a flow of pure helium (3.000 dm^3/h). Subsequently, temperature was elevated up to 350 °C, and dosing of the reactant feed was started. The first GC analysis was commenced after 15 min time-on-stream, and the further analyses were recorded at 40 min time intervals within the total reaction time of 7 h. The catalytic performance, expressed as conversion of EB, yield of styrene, and selectivity towards a particular reaction product, was evaluated by Eqs. (1)–(3):

$$C_{EB} = \frac{\dot{n}_{EB,0} - \dot{n}_{EB}}{\dot{n}_{EB,0}} \cdot 100\% \quad (1)$$

$$Y_i = \frac{\dot{n}_i}{\dot{n}_{EB,0}} \cdot 100\% \quad (2)$$

$$S_i = \frac{Y_i}{C_{EB}} \cdot 100\% \quad (3)$$

where:

C_{EB} – conversion of ethylbenzene [%];
$\dot{n}_{EB,0}, \dot{n}_{EB}$ – molar flow rate of EB in the inlet and outlet stream, respectively [mol/s];
Y_i – yield of *i* product [%];
$\dot{n}_i$ – molar flow rate of EB transformed into *i* product [mol/s];
S_i – selectivity to *i* product [%].

For the sake of comparison of the catalytic activity of the studied materials with catalysts tested by other researchers under different reaction conditions, the *a* comparative parameter was calculated from Eq. (4) [18,40,41]:

$$a = \frac{X_{EB} \cdot \dot{n}_{EB,0}}{W} \left[\frac{\mu mol}{g_{cat} \cdot s}\right], \quad (4)$$

where:

X_{EB} – conversion of EB expressed as a mole fraction [mol/mol];
W – initial mass of a catalyst [g].

3. Results and discussion

3.1. Effectiveness of PFA deposition in SBA-15 pore system

The effectiveness of accumulation of PFA inside mesochannels of SBA-15 was studied by means of TG under the oxidative atmosphere (air). The TG curves recorded for the studied PFA/SBA-15 composites together with the determined real vs. intended polymer/silica ratios are presented in Fig. 1.

Obviously, the conditions of PFA deposition resulted in relatively high degrees of polycondensation of FA within the whole range of FA concentrations (the real effectiveness of PFA deposition varied between 62% (for PFA/S-0.50) and 88% (for PFA/S-1.50) in relation to the intended values). This is in line with our previous results [18,38]. It should, however, be noted that for all syntheses, the filtrate after separation of a PFA/SBA-15 composite exhibited an amber-like color, evidencing the presence of water-soluble oligomeric furfuryl entities. Therefore, part of the monomer was lost and the lower real amounts of polymer in the composites compared to the intended ones are understandable [18,38].

3.2. Textural characteristic of C/S-x composites and C-x replicas

The textural parameters of SBA-15, SBA-15_850, C/S-*x* carbonizates and ultimate C-*x* replicas were investigated by means of low-temperature adsorption-desorption of nitrogen. The relevant isotherms together with the corresponding pore size distribution curves are shown in Fig. 2.

All the isotherms collected for SBA-15 and carbonizates (Fig. 2A) demonstrate similar behavior, characteristic of the type IV(a) as classified by IUPAC [42]. Both pure silica and the carbonizate with the lowest PFA loading (C/S-0.50) feature the well distinguished H1 hysteresis loop indicative of the delayed capillary condensation of nitrogen in the mesopores, while the shape of the loop for the higher-loaded composites (i.e. C/S-1.00–C/S-2.00) changes into the H2(a) type with the distinctive closure point at $p/p_0 = 0.43$ (in Fig. 2A marked by asterisks), notwithstanding the content of carbon in the composite [18,37]. This effect is due to the cavitation of the adsorptive, which takes place in partially-blocked mesopores and it is manifested by an artificial rapid drop of nitrogen uptake in the desorption branch at the relative pressure range of 0.40–0.50 [42,43]. In such cases, the closure point of isotherm remains almost irrespective of the real pore dimensions. Therefore, in order to avoid the presence of artificial peaks on PSDs, the NLDFT curves for parent silicas and carbonizates were calculated for the adsorption branches of the isotherms (as an example, see Fig. 2A′–b; conspicuous artificial peak in BJH calculated from the desorption branch at 3.7 nm; Table 1).

In the case of the pristine SBA-15 matrix, the pronounced capillary condensation step, manifested by a rapid increase in nitrogen uptake, occurs at $p/p_0 = 0.70–0.75$, whereas for all the carbonizates a slight shift towards lower relative pressures (p/p_0 = 0.60–0.70) is observed (Fig. 2A). This shift arises from the shrinkage of the SBA-15 framework caused by the high-temperature treatment (carbonization at 850 °C), what is evident by comparison of the isotherms recorded for carbonizates and SBA-15_850 (cf. Fig. 2A) [38]. An increase in the content of the carbonized polymer inside the pore system causes a gradual stricture of the hysteresis loop. As mentioned above, the character of desorption branch for the C/S-1.00, C/S-1.25, and C/S-1.50 samples (i.e. shift of

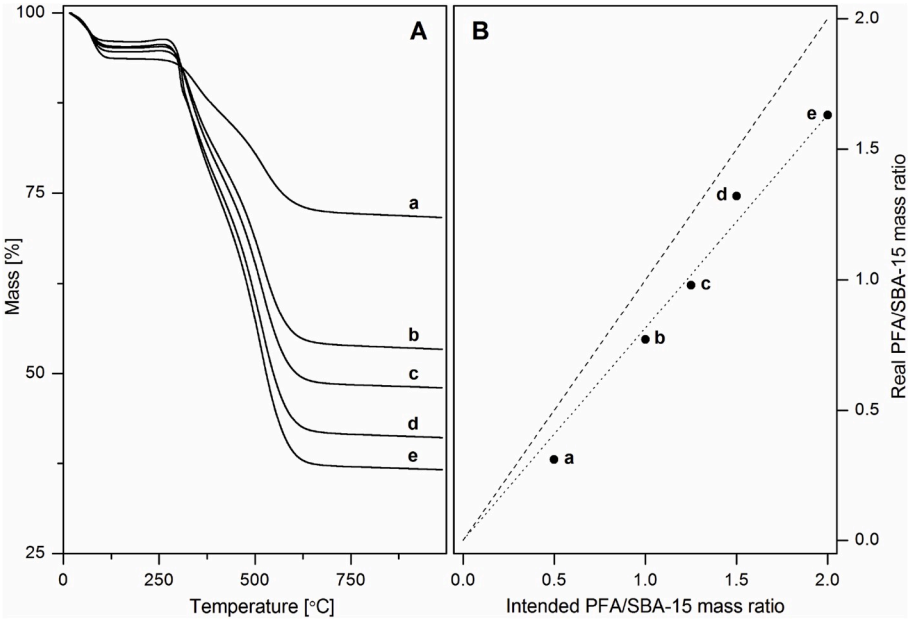

Fig. 1. TG measurements at the air atmosphere for the PFA/S-*x* composites of various PFA/SBA-15 mass ratios (A), and effectiveness of poly(furfuryl alcohol) deposition in the SBA-15 pore system, expressed as a real PFA/SBA-15 mass ratio (B): $x = 0.50$ (a), $x = 1.00$ (b), $x = 1.25$ (c), $x = 1.50$ (d), and $x = 2.00$ (e).

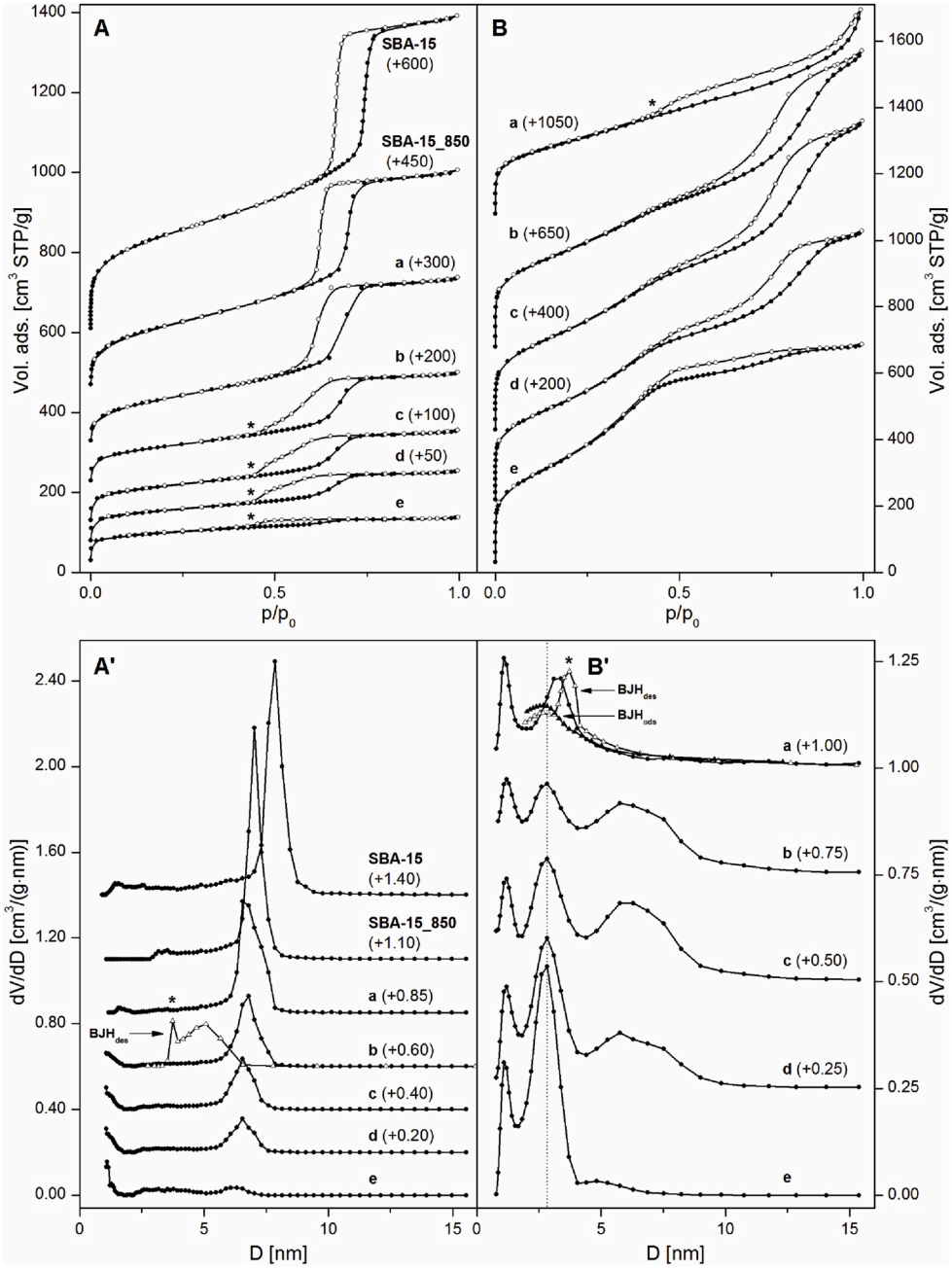

Fig. 2. N_2 adsorption (filled circles) – desorption (open circles) isotherms collected for SBA-15, SBA-15_850, C/S-*x* carbonizates (A), C-*x* replicas (B), and corresponding PSDs (A′ and B′, respectively): $x = 0.50$ (a), $x = 1.00$ (b), $x = 1.25$ (c), $x = 1.50$ (d), and $x = 2.00$ (e) (vertically offset for clarity) (the isotherms closure points at $p/p_0 = 0.43$, and the consequent artificial peaks on BJH PSDs calculated from the desorption branch marked by asterisks).

closure points towards the constant relative pressure of $p/p_0 = 0.43$) suggests the impeded, cavitation-induced evacuation of the adsorptive through the constricted mesopores, what, in turn, is indicative of the formation of the irregular polymer plugs inside the mesochannels. Thus, it can be inferred that the used procedure of the deposition of moderate amounts of PFA does not favor the formation of a homogeneous film cladding the mesopore walls of silica matrix. Nevertheless, for the highest polymer-loaded sample (i.e. C/S-2.00), the hysteresis loop becomes almost invisible. This clearly evidences serious filling of the pore system with the carbon precursor [18].

The pristine SBA-15 material shows a narrow pore size distribution with the maximum centered at 7.9 nm. For the SBA-15 material annealed at 850 °C this maximum shifts towards lower diameter (7.0 nm) (cf. Fig. 2A′). Similarly, the studied C/S-*x* carbonizates reveal the presence of the mesopores uniform in a diameter of 6.3–6.8 nm (Fig. 2A′). The PSDs of the carbonizates disclose two interesting effects, namely: (i) no further shift of the maximum of PSD towards lower pore widths with the increasing polymer content, and (ii) a gradual decrease in the intensity of PSD maximum caused by the progressive pore filling with PFA. These effects clearly suggest the random accumulation of PFA in the SBA-15 pores, i.e. certain channels could be filled completely, while others are partially blocked by small polymer domains formed at the pore mouths and impeding the further filling of SBA-15 mesochannels with carbon precursor [38]. Nonetheless, the increase in PFA content results in a gradual decrease in the amount of these partially plugged pores.

As anticipated, the introduction of the polymer into the pore system of SBA-15 followed by carbonization influenced noticeably the textural

Table 1
Textural and structural parameters of SBA-15, SBA-15_850, C/S-*x* carbonizates, and corresponding C-*x* replicas.

Sample	S_{BET} ($S_{ext.}$) [m^2/g]	S_{micro} [m^2/g] *t*-plot	V_{total} [cm^3/g] s-p	V_{micro} [cm^3/g] α_s	$V_{meso\ I}$ [cm^3/g]	$V_{meso\ II}$ [cm^3/g]	$V_{meso\ I+II}$ [cm^3/g][c]	D [nm]	a_{100} [nm]	$w_{sil.}/w_{carb.}$[d] [nm]
SBA-15	848 (125)	56	1.21	0.03	1.03[a]	–	1.18	7.9	10.8	2.9
SBA-15_850	610 (74)	0	0.85	0.00	0.75[a]	–	0.85	7.0	9.6	2.6
C/S-0.50	474 (53)	18	0.67	0.01	0.59[a]	–	0.66	6.6	9.6	–
C/S-1.00	390 (33)	90	0.46	0.05	0.37[a]	–	0.41	6.8; (5.1)[f]	9.6	–
C/S-1.25	384 (30)	126	0.39	0.06	0.29[a]	–	0.33	6.6	9.4	–
C/S-1.50	343 (20)	139	0.31	0.07	0.21[a]	–	0.24	6.6	9.3	–
C/S-2.00	317 (8)	167	0.21	0.08	0.11[a]	–	0.13	6.3	9.3	–
C-0.50	858	140	0.91	0.10	–	0.81	0.81	1.1; 3.2; (2.7)[f]	–	–
C-1.00	1147	117	1.38	0.11	0.48[b]	0.79[b]	1.27	1.2; 2.8; 5.8	–	–
C-1.25	1203	92	1.45	0.11	0.53[b]	0.81[b]	1.34	1.2; 2.8; 5.8; (3.7)[e]	9.5	7.2
C-1.50	1173	71	1.26	0.11	0.64[b]	0.51[b]	1.15	1.2; 2.8; 5.8; (4.0)[e]	9.4	6.9
C-2.00	1318	35	1.05	0.11	0.86[b]	0.08[b]	0.94	1.2; 2.8; 4.8; (4.5)[e]	9.3	6.2

[a] α_s model.
[b] calculated based on Lorentz deconvolution of PSDs (cf. Fig. 4A).
[c] V_{total}–V_{micro}.
[d] pure silica wall thickness ($w_{sil.}$), and carbon replica *nanorod* diameter ($w_{carb.}$), calculated based on Eqs. (S1), and (S2), respectively.
[e] CMK-3 primary mesopore diameter calculated based on Eq. (S3).
[f] BJH model, desorption branch (cf. Fig. 2A′).

parameters of the composites (cf. Table 1).

The gradual drop in the BET surface area (S_{BET}) and total pore volume (V_{total}) with increasing amount of polymer clearly evidences the successful incorporation of PFA into the mesoporous structure of silica matrix. The slight growth in the micropore volume (V_{micro}) and considerable increase in the micropore surface (S_{micro}) with the raising polymer content is understandable, as it arises from the development of the intrinsic microporosity of the carbonized PFA (cf. Fig. 3; Table 1) [18].

The simultaneous decrease in the primary mesoporosity of SBA-15 ($V_{meso\ I}$) additionally evidences the progressive blocking of the pore system of SBA-15. The external surface area ($S_{ext.}$) of C/S-*x* carbonizates calculated according to the α_s model decreases with the increasing polymer content from 53 m^2/g for C/S-0.50 to 8 m^2/g for C/S-2.00. This suggests the accumulation of the polymer also on the external surface of the silica particles [18,38]. It should be, however, underscored that the covering of the external surface of silica grains with PFA does not entail the conglomeration of the composite particles as one would suppose. This is proven by the absence of an additional porosity, which could be created between the coalesced particles (cf. Fig. 2A). Besides, the TEM micrographs taken for the chosen carbon replicas additionally indicate that the morphology of the pristine matrix remains unaltered throughout the entire replication procedure (cf. Fig. 6).

The nitrogen isotherms collected for the ultimate carbon replicas are presented in Fig. 2B. All of them may be classified as IV(a) type according to IUPAC [9,18,42]. Apart from the C-0.50 sample, the others exhibit the H2(b) hysteresis loop [42]. The observed specific, well pronounced two inflections in the adsorption branches of the isotherms recorded for the C-1.00, C-1.25, C-1.50, and C-2.00 carbons at p/p_0 = 0.3–0.5 and 0.7–0.9, are associated with two steps of capillary condensation, what, in turn, indicates the existence of two individual mesopore systems. This is clearly reflected in the respective PSDs presented in Fig. 2B′. All these PSDs exhibit the maxima centered at 1.1–1.2 nm (attributed to the inherent microporosity of the carbonized PFA) and 2.8 nm (ascribed to the voids between the carbon *nanorods*). The third broad peak on PSD observed for the C-1.00, C-1.25, and C-1.50 materials originates from the coalescence of the adjacent SBA-15 pores, which underwent merely partially filling with the polymer. Thus, for the samples with the PFA/SBA-15 mass ratio of 1.00–1.50 this size ranges roughly within 4.5–10.0 nm (with a maximum at ca. 5.8 nm), while the C-2.00 sample shows a narrower and scarcely visible peak at 4.0–7.0 nm (centered at 4.8 nm). As the PSDs for C-1.00, C-1.25, C-1.50, and C-2.00 exhibit two broad and overlapping peaks in the mesopore range, in order to calculate both the mesopore volumes separately, the QSDFT profiles

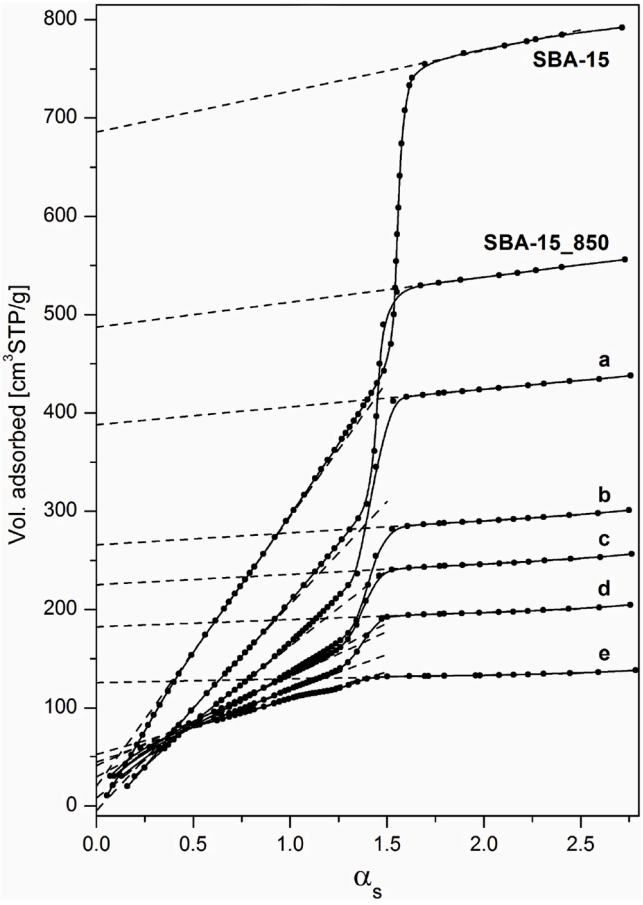

Fig. 3. Comparative α_s plots for pristine SBA-15, SBA-15_850, and C/S-*x* carbonizates: *x* = 0.50 (a), *x* = 1.00 (b), *x* = 1.25 (c), *x* = 1.50 (d), and *x* = 2.00 (e).

were deconvoluted using Lorentz algorithm, as shown in Fig. 4A. The computed values are compiled in Table 1, while the particular fractions of pores in the total pore volumes of the replicas are depicted in Fig. 4B.

In the case of the samples with the intended PFA/SBA-15 ratios of 1.00–2.00 the volume of the primary mesopores ($V_{meso\ I}$) rises gradually with the increasing polymer content, while the volume of the larger voids ($V_{meso\ II}$) decreases systematically. Surprisingly, the specific surface area (S_{BET}) of carbon replicas remains within the range of 1150–1320 m^2/g notwithstanding the content of the carbon precursor. Combining these remarks one may infer that the method of introduction of PFA inside the pore system of SBA-15 by precipitation polycondensation results in the formation of carbon replicas featuring the presence of a complex pore structure in the mesopores region. Namely, as already mentioned, the replicas exhibit the presence of some random inhomogeneities (larger voids) in the structure. In a boundary case, i.e. for the samples derived from the carbonizates with the low PFA content, these inhomogeneities preclude the formation of stably merged, well-ordered 3D mesostructure.

The hysteresis loop on the isotherm of replica derived from the C/S-0.50 carbonizate (i.e. C-0.50) has the H4 shape typical of micro-mesoporous solids with the slit-shaped pores (cf. Fig. 2B) [42]. Most likely, in this case the ordered structure of carbon framework underwent the partial collapse after removal of the silica scaffolding. The material exhibits the relatively high surface area of 858 m^2/g, total pore volume of 0.91 cm^3/g, and main QSDFT mesopore size of 3.2 nm. Interestingly, the pore size distributions computed based on the BJH model (both adsorption and desorption branches of isotherm) show minor maxima centered at about 2.7 nm (obviously, the distinctive sharp peak at 3.7

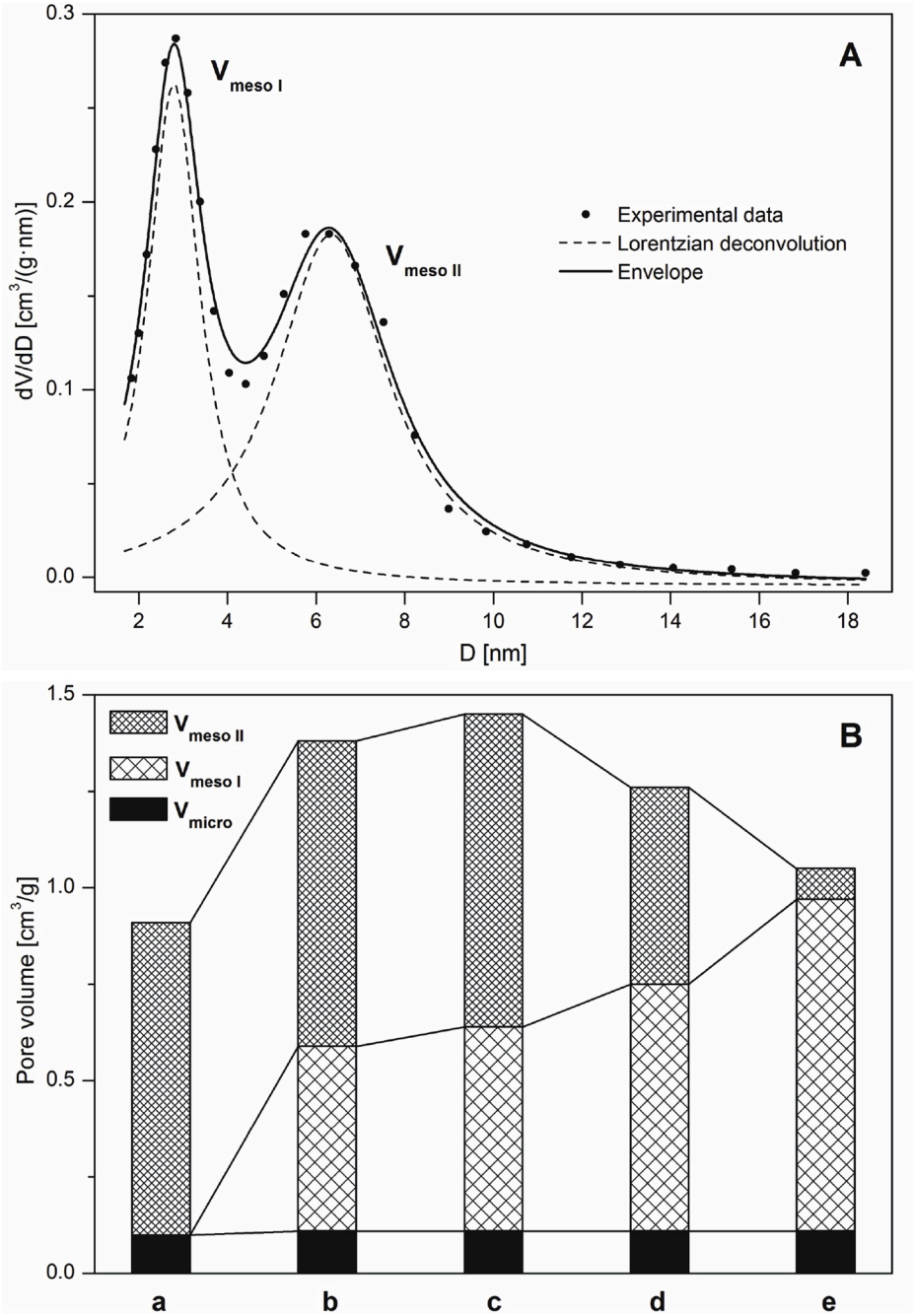

Fig. 4. Exemplary Lorentz deconvolution of PSD curve of C-1.25 sample (A), and contributions of particular pore volumes to V_{total} of C-x replicas (B): $x = 0.50$ (a), $x = 1.00$ (b), $x = 1.25$ (c), $x = 1.50$ (d), and $x = 2.00$ (e). (the lines connecting the columns added to guide the eyes).

nm in BJH desorption PSD is an artifact) [42]. Thus, combining the behavior of the nitrogen isotherm (i.e. closure point at $p/p_0 = 0.43$) and PSD, it should be noted that the certainty of QSDFT model in this particular case may be questionable. For this reason, care must be taken when comparing these results with the other samples within the series. It is noteworthy that in this case no larger mesopores (with diameters ranging within 4.5–10.0 nm) are observed. This clearly confirms the above supposition: no long-ranging structure of this material arises from advanced disintegration of the three–dimensional carbon framework after removal of the silica scaffolding. Besides, the lowest cumulative mesopore volume ($V_{meso\ I+II}$) within the series noticed for C-0.50 carbon additionally supports the foregoing remarks.

More interestingly, contrary to our conjectures, the micropore surface area of the replicas decreases systematically with the increasing amount of PFA (cf. Table 1). Considering the micropore surface area of the C/S-2.00 carbonizate and the respective C-2.00 replica ($S_{micro} = 167$ and 35 m^2/g, respectively), one may conclude that the removal of silica matrix resulted in a severe decrease in S_{micro}. A plausible explanation of this effect may be the formation of micropores between carbon rods and silica matrix during carbonization caused by the differences in the shrinkage effect of both materials (i.e. a discrepancy in the scale of contraction between carbon and silica when subjected to thermal treatment). This is evident when considering that after leaching of silica these voids disappear. Interestingly, the micropore volumes of the replicas remain constant notwithstanding the level of loading the pore system of SBA-15 with PFA. Thus, deposition of PFA inside the pore system of the silica matrix does not influence microporosity of the final replicas. As stated above, this microporosity comes purely from the inherent micropore structure formed in the PFA when carbonized [18].

3.3. Structure and morphology of C/S-x composites and C-x replicas

The above presented considerations are additionally supported by the X-ray diffraction patterns collected for the studied materials (Fig. 5).

The XRD pattern recorded for pristine SBA-15 (Fig. 5A) exhibits three well resolved reflections at 2θ of 0.94°, 1.59° and 1.83°, indexed as (1 0 0), (1 1 0), and (2 0 0) planes, respectively, and ascribed to the p6mm space group [44,45]. The calculated d_{100} interplanar spacing equals 9.4 nm and thereby the a_{100} lattice parameter (being the center-to-center distance of the adjacent pores) is 10.8 nm (Table 1). The shrinkage effect in the case of the SBA-15_850 sample is clearly reflected in the calculated d_{100} and a_{100} parameters (8.4 and 9.6 nm, respectively), what is in full accordance with the PSDs (cf. Table 1; Fig. 2B). The XRD patterns collected for the carbonizates (Fig. 5A) indicate that the hexagonal array was preserved throughout the entire synthesis procedure (i.e. deposition of polymer and carbonization). The lattice parameters of the C/S-*x* composites and the corresponding replicas are listed in Table 1. The values of a_{100} for the carbonizates are about 1 nm lower when compared with pristine SBA-15, what turns out to be plausible in view of the structural parameters calculated for SBA-15_850 (cf. Table 1) [28,31,38].

The XRD patterns collected for the series of carbon replicas (Fig. 5B) reveal that the formation of a stable, well-ordered replica requires a certain minimal level of loading of SBA-15 pores with the carbon precursor. As seen, in the case of the employed synthetic route, the boundary minimal mass ratio of PFA/SBA-15 providing the successful replication of silica structure (i.e. the XRD pattern features the typical set of three reflections), is equal to 1.25. For the materials with lower polymer contents (i.e. C-0.50, and C-1.00), the XRD patterns exhibit lack of the relevant reflections suggesting the aforementioned collapse of the carbon mesostructure. The structural parameters of the successfully formed replicas are gathered in Table 1. The carbon *nanorods* diameters ($w_{carb.}$) were calculated based on a simple geometrical relation employing the d_{100} interplanar spacings and the respective micro- and mesopore volumes (cf. Eq. (S2)). Although the carbon content in the composites does not substantially affect the unit cell size, a slight tendency of diminishing of the carbon *nanorods* diameter with an increase in the level of loading of SBA-15 with PFA is observed. For the C-1.25, C-1.50, and C-2.00 samples, the *nanorods* diameters of 7.2, 6.9, and 6.2 nm, respectively, were calculated. These values are in compliance with the pore size of the counterpart SBA-15_850 silica.

TEM images for chosen resulting replicas (Fig. 6) taken

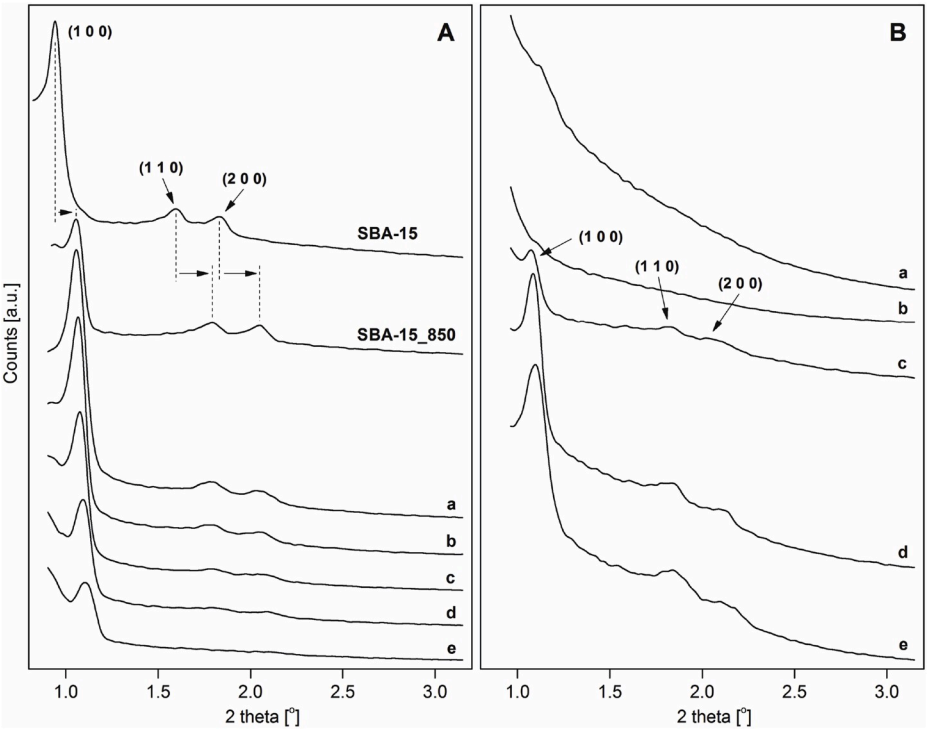

Fig. 5. Low-angle XRD patterns collected for pristine SBA-15, SBA-15_850, C/S-*x* carbonizates (A), and corresponding C-*x* replicas (B): $x = 0.50$ (a), $x = 1.00$ (b), $x = 1.25$ (c), $x = 1.50$ (d), and $x = 2.00$ (e).

perpendicular to the *nanorods* clearly show their hexagonal arrangement. The micrographs confirm also the maintenance of the structural architecture and particle morphology characteristic of SBA-15. It should be noted that the samples originated from the carbonizates with higher PFA content (i.e. C-1.50, and C-2.00) exhibit the presence of an amorphous carbon shell covering the outer surface of the grain (cf. Fig. 6C and D; the places indicated by arrows). This effect is caused by the superficial deposition of the excess PFA on SBA-15, as reported elsewhere [18,38].

3.4. Mechanism of formation of carbon replicas structures

The thorough study on the evolution of the textural and structural features of the materials allowed us to propose the general pathway of formation of the ordered carbon structures by the precipitation polycondensation of FA in a water slurry of SBA-15 with increasing amounts of carbon precursor. The mechanism of formation of the regular structures of CMK-3 may be summarized in the four following steps:

(i) In the case of the composite synthesized at the lowest PFA/SBA-15 ratio (i.e. PFA/S-0.50), the polymeric domains accumulate throughout the silica matrix pore system randomly. Only a limited fraction of mesopores is completely filled with PFA, while the others underwent partial filling with the carbon precursor. The removal of the SBA-15 matrix from the C/S-0.50 material after carbonization results in an advanced collapse of the carbon framework. This in turn results in the formation of smaller carbon particles exhibiting abundant intrinsic microporosity and vestigial mesoporosity formed in the place of the leached silica walls. As a consequence, the ultimate carbon structure (C-0.50) exhibits the unordered spatial structure (cf. Fig. 2B′–a; Fig. 5B–a; Fig. 7a).

(ii) The higher amount of the monomer available in the synthesis medium results in a higher degree of SBA-15 pore filling (PFA/S-1.00), but the structuring of the carbon framework formed in the C/S-1.00 carbonizate is still not sufficient to merge perfectly the 3D array of the corresponding C-1.00 replica. After the contact with silica leaching agent, the structure undergoes a partial disintegration along the weakest links (i.e. partially filled adjacent pores). However, the moderate degree of pore filling enables the creation of somewhat larger domains with a bimodal mesoporosity formed by the coalescence of the adjacent SBA-15 pores unfilled completely with the polymer. Nevertheless, the relatively small dimensions of these domains still result in the lack of long-range ordering, what is additionally reflected in the XRD results (cf. Fig. 2B′–b; Fig. 5B–b; Fig. 6A; Fig. 7b).

(iii) The adjacent carbon *nanorods* for the samples C/S-1.25, and C/S-1.50 are bridged by the narrower carbon rods. Such structuring turns out to be sufficient to maintain the merged 3D framework of the C-1.25, and C-1.50 replicas. This allowed us to calculate the replication fidelity indices for these samples. The RFI of 0.59, and 0.68 were found for C-1.25, and C-1.50 replicas, respectively. It should be, however, underscored that the presence of a large number of partially filled pores in the siliceous matrix still results in a formation of bimodal mesoporosity in both discussed replicas (cf. Fig. 2B′–c,d; Fig. 5B–c,d; Fig. 6B and C; Fig. 7c,d). As mentioned in our recent paper, we reported on the synthesis of porous structures analogous to CMK-5 calling them "*pseudo*-CMK-3" [38].

(iv) The micro- and mesopore structure of SBA-15 in the PFA/S-2.00 composite is almost completely filled with polymer. As a consequence, the resulting C-2.00 replica exhibits only one peak in the mesopore region of the PSD and a set of the typical well pronounced three diffraction reflections characteristic of the p6mm symmetry. The homogenous monomodal mesopore system is formed in the place of the removed silica walls. In this case, the RFI parameter was 0.94, proving almost perfect negative replication of the SBA-15 structure (i.e. RFI = 1.00) (cf. Fig. 2B′–e; Fig. 5B–e; Fig. 6D; Fig. 7e). This indicates that the higher is the loading of the pore system of SBA-15 with PFA the larger is the similarity of the structure of the resulting material to the ideal inverse replica of the pristine silica matrix.

The successive development of the primary mesoporosity of replicas with increasing level of SBA-15 pore filling clearly reflects the gradual formation of the regular CMK-3 replica structure (cf. Table 1; Fig. 4B). Therefore, combining the foregoing, it may be concluded that the random accumulation of PFA in the SBA-15 structure precludes the possibility of synthesis of regular CMK-5 structures employing this procedure; however, the obtained porous structures called "*pseudo*-CMK-3" may be favorable in view of their potential applications in adsorption and catalysis [38].

3.5. Surface composition of carbon replicas

The nature and quantity of the oxygen-containing entities present in the fresh carbon replicas were determined by means of TPD and XPS measurements. The comprehensive analysis of the results brought

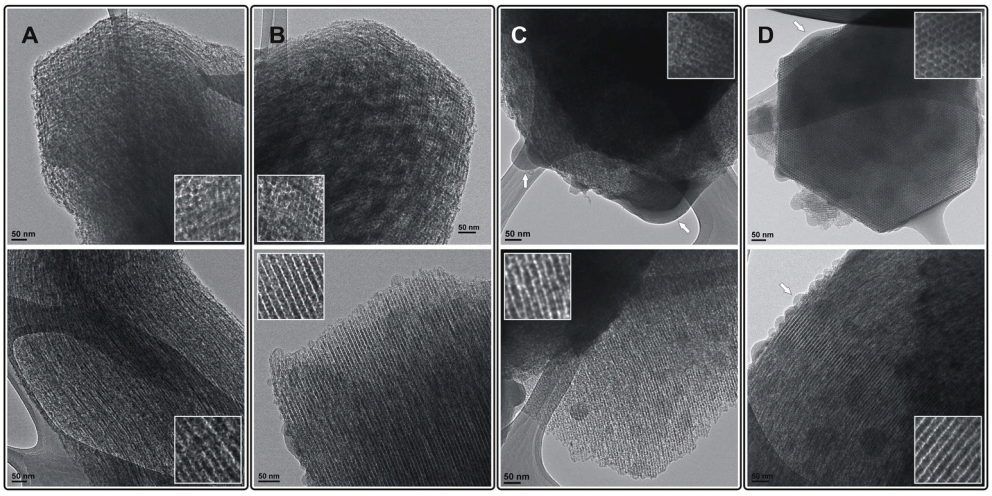

Fig. 6. TEM images taken perpendicular (top) and parallel (bottom) to the *nanopipes/nanorods* of C-*x* replicas: $x = 1.00$ (A), $x = 1.25$ (B), $x = 1.50$ (C), and $x = 2.00$ (D). The arrows indicate the amorphous carbon shell covering the surface of silica grains.

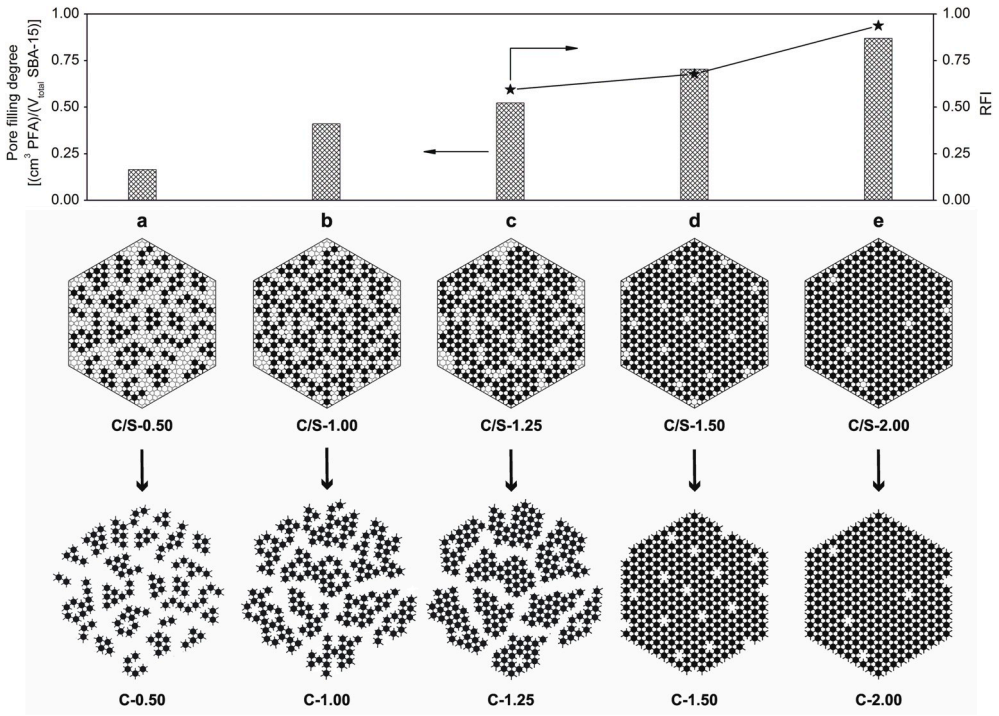

Fig. 7. Replication fidelity indices (RFI) with regard to the pore filling degree (top), and postulated mechanism of incorporation of PFA into SBA-15 pore system together with the fates of carbon frameworks after silica removal (bottom).

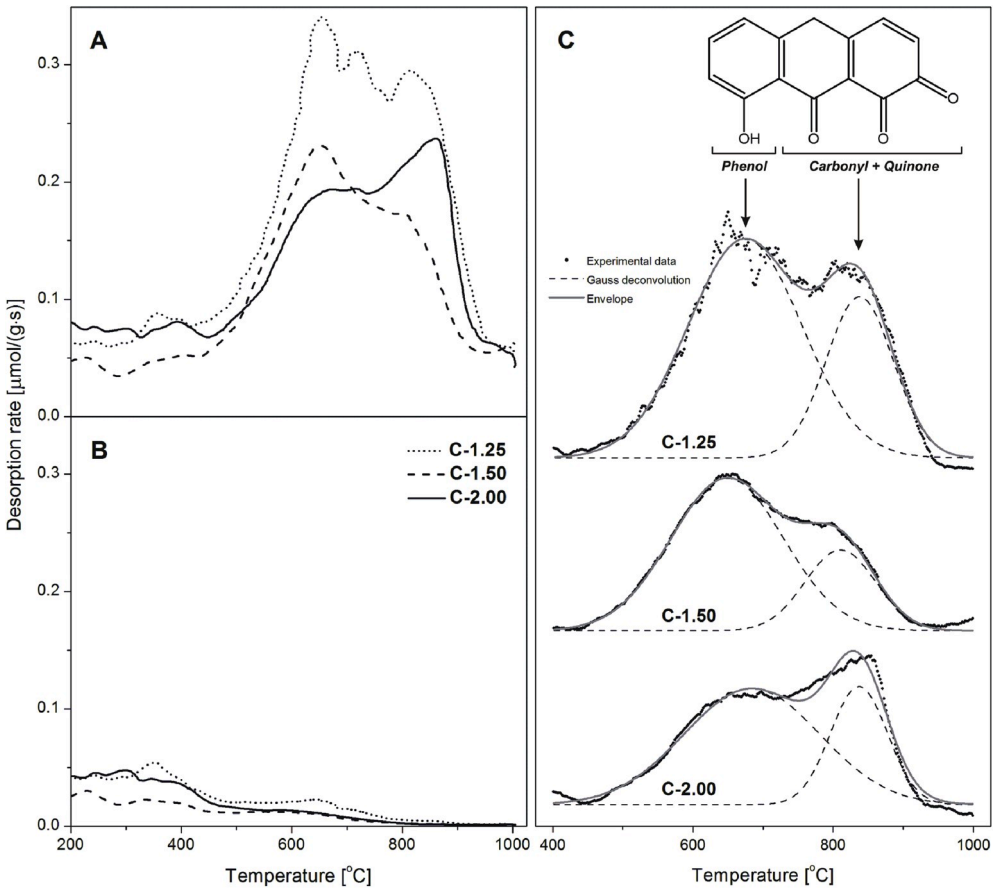

Fig. 8. Temperature-programmed desorption profiles of CO (A), and CO_2 (B) for chosen fresh carbon replicas, and Gauss deconvolution of the CO profiles (C).

insight into the composition of carbon replica on the entire surface (i.e. external and internal; TPD) as well as on the outermost few atomic layers of the accessible surface of material (XPS). The recorded CO- and CO_2-TPD profiles measured within a temperature range of 200–1000 °C are depicted in Fig. 8, while the total concentrations of oxygen-containing moieties which decompose evolving CO and CO_2 are summarized in Table 2.

The maximum of CO_2 desorption rate of a poor intensity observed below 400 °C reveals that only a minor part of the oxygen-containing species exists in the form of the least stable carboxyl groups [40,41,47]. Interestingly, lack of the characteristic peaks at 620–700 °C, and 500–580 °C in the CO_2-TPD profiles indicates the absence of lactone and anhydride entities. Besides, the lack of latter one is additionally evidenced by the absence of the peak component in the CO-TPD at 500–580 °C (as the anhydride groups decompose into both CO and CO_2) [40,41,47].

The CO-TPD profiles collected for all the studied replicas are mutually similar, exhibiting in the curve-resolved form two well distinguished maxima centered at around 670 °C, and 850 °C. These peaks correspond to the decomposition of phenols, and carbonyl/quinone species, respectively. It is noteworthy that the content of the carbonyl moieties for all samples reaches around 80% in relation to the total oxygen content (cf. Table 2). The highest total oxygen content of 1.05 mmol [O]/g was noted for the C-1.25 replica. Generally, the TPD results clearly reveal that the studied carbon replicas contain thermally stable functional oxygen-containing moieties.

The contributions of particular oxygen- and carbon-containing superficial groups determined for chosen replicas by XPS are collected together with the respective binding energies in Table 3, while the relevant C 1*s*, and O 1*s* regions of XPS spectra are gathered in Fig. S1.

The C 1*s* core level spectra were fitted with four peaks as follows: (i) carbon atoms of sp^2 and sp^3 hybridization in graphitic and disordered moieties (E_b = 284.4 eV), (ii) C–OH (E_b = 286.4 eV), (iii) C═O (E_b = 287.4 eV), and (iv) COOH (E_b = 288.4 eV) [18,34,48–50]. The O 1*s* spectra were deconvoluted into four following components: (i) carbonyl groups (C═O) (E_b = 530.8 eV), (ii) hydroxyl (C–OH), and oxygen double bonded to carbon atom in carboxyl groups (C═OH) (E_b = 533.0 eV), (iii) oxygen single bonded to carbon atom in carboxyl groups (COOH) (E_b = 534.4 eV), and (iv) oxygen atoms in adsorbed water (E_b = 537.0 eV) [18,48,49]. As seen in Table 3, the surface composition of the studied replicas is substantially influenced by an amount of carbon precursor accumulated in the SBA-15 pore system. The concentration of sp^2 and sp^3 carbon rises with an increase in the degree of pore filling of silica with PFA. As a consequence, the concentration of oxygen-containing moieties decreases. The majority of these entities exists as a carbonyl/quinone and hydroxyl (phenol) groups which may act as catalytic sites. It is interesting to consider that all surface moieties may originate either from the oxygen being an original constituent of a carbon precursor (as oxygen contributes 32.6 wt% of FA) or from the re-oxidation of freshly carbonized sample after exposure to atmospheric air, as it is well known that such materials exhibit high reactivity towards oxygen [18,46–48]. This prompted us to do a closer inspection of the real genesis of these oxygen moieties. For this purpose, employing the thermobalance, we carried out an experiment simulating carbonization of PFA/S-2.00 composite followed by exposure to air (at 30 °C), and subsequent temperature-programmed desorption under the nitrogen atmosphere (cf. Supplementary Information, Fig. S2 together with a thorough discussion). Considering the TPD results (cf. Fig. 8; Table 2), it is easy to calculate that in the case of the C-2.00 replica, the desorption of both carbon oxides results in a mass loss of ca. 2.1%. On the other hand, the mass increase noticed during the step of exposure to air reached roughly 2.5–3.0% in the reference experiment (cf. Fig. S2B; the mass of carbonizate normalized to the content of carbon; the amount of adsorbed water was subtracted). Combining these results one can conclude that the majority of the surface oxygen species is formed when the freshly carbonized sample comes into contact with air.

Table 2
Amounts of CO_2 and CO evolved during the TPD experiments for chosen fresh carbon replicas.

Sample	CO [mmol/g]	CO_2 [mmol/g]	Total oxygen [mmol [O]/g]	CO/CO_2	CO/total oxygen
C-1.25	0.83	0.11	1.05	7.5	0.79
C-1.50	0.55	0.06	0.67	9.2	0.82
C-2.00	0.62	0.09	0.80	6.9	0.78

3.6. Catalytic activity of carbon replicas in oxidative dehydrogenation of ethylbenzene

The oxidative dehydrogenation of ethylbenzene is considered to be a prospective alternative for contemporaneous industrial technology of production of styrene mainly due to its favorable energy balance. In contrary to the highly endothermic equilibrium dehydrogenation technology ($\Delta H^\circ = +117.6$ kJ/mol), ODH of ethylbenzene is an irreversible and strongly exothermal reaction ($\Delta H^\circ = -124.3$ kJ/mol) [51].

The use of carbon materials as catalysts for ODH processes has attracted a great interest of researchers since the early 1980's, when Emig and Hofmann reported on the mechanism of so-called *active coke*, which allowed to explain the high catalytic activity upon the formation of a superficial coke layer after the initial period of the reaction run [51]. The effect of gradual activation with time-on-stream was correlated with the formation of the quinone moieties [51,52]. The postulated mechanism of *active coke* assumes the role of the quinone/hydroquinone redox system acting as real active centres [51,52].

The abundant concentration of phenolic and carbonyl/quinone groups evidenced by TPD and XPS study makes the replicas excellent candidates for the catalytic purposes of ODH. Three selected, well-ordered carbon replicas (namely C-1.25, C-1.50, and C-2.00) were tested in the ODH of EB in the presence of oxygen at the O_2: EB ratio of 1.0 and at the reaction temperature of 350 °C, as it was found to be favorable in our previous studies [18,49]. The catalytic parameters recorded during a 7 h catalytic run are depicted in Fig. S3. Apparently, all the investigated samples exhibit a high catalytic activity. The main products formed over the catalysts were styrene and CO_x, while others (i.e. benzene, toluene, and coke) were produced with a cumulative selectivity lower than 1.4%. The reaction system achieved a steady state after ca. 4–5 h. The initial and steady-state catalytic performance (after 15, and 360 min of time-on-stream, respectively) are compared in Table 4.

The highest initial conversion of EB (29.1%) was denoted for the C-2.00 catalyst, whereas the utmost selectivity towards styrene (92.6%) was found over the C-1.25 sample. It should be underscored that the selectivity to styrene in the latter case increases gradually with time-on-stream of 1.4%, while for the other samples it declines slightly (see Fig. S3; Table 4). Interestingly, the TPD and XPS study reveal that the C-1.25 material exhibits the highest content of oxygen-containing surface entities among the studied catalysts (cf. Table 2; 3). Apparently, the concentration of oxygen-containing surface groups affects substantially the catalytic performance of the replicas. This additionally supports the postulated mechanism of *active coke*. Furthermore, the C-1.25 replica exhibits the lowest selectivity to CO_x and utmost selectivity to styrene, while its selectivity to the trace products decreases with time-on-stream from 1.4 to 0.3% (cf. Fig. S3; Table 4). All studied catalysts undergo a gradual deactivation with time-on-stream. This effect may be due to the formation of the carbon deposit (catalytically inactive) onto the surface, which causes the impeded accessibility of the reactants to the catalytic sites, as reported earlier [49]. Nevertheless, the least deactivation degree of 10.7% as compared to the initial, was observed for the C-2.00 catalyst. It is interesting to juxtapose the performance of the C-1.25 and C-2.00 replicas with regard to their mutual textural differences (i.e. the "*pseudo*-CMK-3" structure vs. typical CMK-3 framework, respectively).

Table 3
Concentration of carbon and oxygen species on the surface of fresh replicas determined by XPS.

Sample	Carbon [at.%]				Oxygen [at.%]				CO/CO_2[a]
	C=C sp^2 C–C sp^3	C–OH	C=O	COOH	C=O	OH, COOH	COOH	H_2O ads.	
	284.4 eV	286.4 eV	287.4 eV	288.4 eV	530.8 eV	533.0 eV	534.4 eV	537.0 eV	
C-1.25	94.15	1.98	0.70	0.10	0.70	2.08	0.10	0.20	7.0
C-1.50	94.62	1.97	0.38	0.16	0.38	2.13	0.16	0.21	2.4
C-2.00	95.11	1.68	0.57	0.10	0.57	1.78	0.10	0.08	5.7

[a] calculated based on C 1*s* data.

Table 4
Conversion of EB, selectivity towards styrene, carbon oxides, and other products measured over selected replicas after 15 and 360 min time-on-stream.

Sample	Conversion of EB [%]		Selectivity to styrene [%]		Selectivity to CO_x [%]		Selectivity to other products [%]		$a\left[\frac{\mu mol}{g_{cat} \cdot s}\right]$
	15 min	360 min	15 min	360 min	15 min	360 min	15 min	360 min	
C-1.25	26.3	14.6	92.6	94.0	6.0	5.8	1.4	0.3	1.2
C-1.50	28.6	14.4	91.3	91.0	8.4	8.9	0.3	0.1	1.3
C-2.00	29.1	18.4	91.5	91.2	8.2	8.7	0.2	0.2	1.5

Namely, when considering their prominently different behavior along with the time-on-stream of the ODH run, the impact of the textural features on the catalytic potential of carbon replicas turns out to be evident. Finally, it is also pertinent to mention that the comparative a parameters calculated in ODH of ethylbenzene for the C-1.25, C-1.50, and C-2.00 replicas (1.2, 1.3, and 1.5, respectively; cf. Eq. (4); Table 4) revealed that the latter material surpasses the formerly reported activated carbon (with a = 1.47), as well as carbon nanotubes (a = 0.80–1.12) [18,40,41].

4. Conclusion

This study was aimed at the thorough investigation on the mechanism of accumulation of various amounts of poly(furfuryl alcohol) in the SBA-15 pore system by the previously developed method of precipitation polycondensation of FA in a polar medium (water). A series of CMK-3-like carbon replicas has been synthesized at the polymer/silica mass ratio ranging within 0.50–2.00. The mechanism of deposition of increasing polymer content onto silica surface was elucidated based on a thorough study of the textural and structural parameters of the mother silica matrix, carbonizates and final carbon replicas. It was found that the poly(furfuryl alcohol) accumulates in the SBA-15 pore system in a random manner, i.e. certain channels undergo a complete filling, while others remain partially empty. A plausible explanation of such effect may be the formation of PFA plugs at the pore mouths. Consequently, further incorporation of the polymer to the SBA-15 mesochannels is impeded.

This precludes the feasibility of the synthesis of a regular CMK-5 structure, but facilitates the formation of the "*pseudo*-CMK-3" frameworks, which feature an interesting bimodal mesoporosity (the primary mesopores are the regular ones appearing after silica walls leaching, while the broader secondary pores originate from the coalescence of the adjacent SBA-15 pores, which remained incompletely filled with the polymer). Most likely, the synthesis of the CMK-5 replica requires the incorporation of the catalyst into the silica matrix walls and/or the use of non-polar solvents for the introduction of monomer to silica channel structure, as was reported formerly. The studied CMK-3-like carbon materials exhibited the presence of abundant amounts of the surface oxygen-containing groups, among which the phenolic and carbonyl/quinone ones were dominating. The TG measurement revealed that these entities were formed after contact of freshly carbonized composites with air. Such beneficial surface chemistry was reflected in a promising catalytic performance of these materials in the ODH process, surpassing reported activated carbons and carbon nanotubes. Therefore, the materials seem to be promising candidates for catalytic purposes, especially those requiring the engagement of the surface O-containing moieties.

Declaration of competing interest

The authors declare that they have no known competing financial interests or personal relationships that could have appeared to influence the work reported in this paper.

Acknowledgments

This work was supported by the Polish National Science Centre under the grant no. DEC-2011/01/N/ST5/05595. The research was carried out with the equipment purchased thanks to the financial support of the European Regional Development Fund in the framework of the Polish Innovation Economy Operational Program (contract No. POIG.02.01.00-12-023/08). The research was carried out using the infrastructure of the AGH Centre of Energy, AGH University of Science and Technology.

Appendix A. Supplementary data

Supplementary data to this article can be found online at https://doi.org/10.1016/j.micromeso.2020.110118.

References

[1] S. Tan, W. Zou, F. Jiang, S. Tan, Y. Liu, D. Yuan, Mater. Lett. 64 (2010) 2163–2166.
[2] M. Hartmann, A. Vinu, G. Chandrasekar, Chem. Mater. 17 (2005) 829–833.
[3] H. Zhang, H. Tao, Y. Jiang, Z. Jiao, M. Wu, B. Zhao, J. Power Sources 195 (2010) 2950–2955.
[4] T. Komanoya, H. Kobayashi, K. Hara, W.J. Chun, A. Fukuoka, Appl. Catal. Gen. 407 (2011) 188–194.
[5] N. Mohammadi, H. Khani, V.K. Gupta, E. Amereh, S. Agarwal, J. Colloid Interface Sci. 362 (2011) 457–462.
[6] M. Hartmann, Chem. Mater. 17 (2005) 4577–4593.
[7] R. Ryoo, S.H. Joo, S. Jun, J. Phys. Chem. B 103 (1999) 7743–7746.
[8] R. Ryoo, S.H. Joo, Stud. Surf. Sci. Catal. 148 (2004) 241–260.
[9] A.B. Fuertes, Microporous Mesoporous Mater. 67 (2004) 273–281.
[10] S. Jun, S.H. Joo, R. Ryoo, M. Kruk, M. Jaroniec, Z. Liu, T. Ohsuna, O. Teresaki, J. Am. Chem. Soc. 122 (2000) 10712–10713.
[11] B. Sakintuna, Y. Yürüm, Ind. Eng. Chem. Res. 44 (2005) 2893–2902.
[12] M.W. Anderson, T. Ohsuna, Y. Sakamoto, Z. Liu, A. Carlsson, O. Terasaki, Chem. Commun. 10 (8) (2004) 907–916.
[13] H. Darmstadt, C. Roy, S. Kaliaguine, T.-W. Kim, R. Ryoo, Chem. Mater. 15 (2003) 3300–3307.
[14] Z. Lei, S. Bai, Y. Xiao, L. Dang, L. An, G. Zhang, Q. Xu, J. Phys. Chem. C 112 (2008) 722–731.
[15] S. Che, K. Lund, T. Tatsumi, S. Iijima, S.H. Joo, R. Ryoo, O. Terasaki, Angew. Chem. Int. Ed. 42 (2003) 2182–2185.

[16] A.H. Lu, J.J. Nitz, M. Comotti, C. Weidenthaler, K. Schlichte, C.W. Lehmann, O. Terasaki, F. Shüth, J. Am. Chem. Soc. 132 (2010) 14152–14162.
[17] D. Gu, W. Li, F. Wang, H. Bongard, B. Spliethoff, W. Schmidt, C. Weidenthaler, Y. Xia, D. Zhao, F. Shüth, Angew. Chem. Int. Ed. 54 (2015) 7060–7064.
[18] P. Niebrzydowska, R. Janus, P. Kuśtrowski, S. Jarczewski, A. Wach, A.M. Silvestre-Albero, F. Rodríguez-Reinoso, Carbon 64 (2013) 252–261.
[19] A.B. Fuertes, D.M. Nevskaia, Mater. Chem. 13 (2003) 1843–1846.
[20] A.B. Fuertes, Mater. Chem. 13 (2003) 3085–3088.
[21] Y. Xia, Z. Yang, R. Mokaya, Chem. Mater. 18 (2006) 140–148.
[22] Y. Xia, R. Mokaya, Adv. Mater. 16 (2004) 1553–1558.
[23] Y. Xia, Z. Yang, R. Mokaya, Nanoscale 2 (2010) 639–659.
[24] A.-H. Lu, F. Schüth, Adv. Mater. 18 (2006) 1793–1805.
[25] T. Yokoi, S. Seo, N. Chino, A. Shimojima, T. Okubo, Microporous Mesoporous Mater. 124 (2009) 123–130.
[26] S.H. Joo, S.J. Choi, I. Oh, J. Kwak, Z. Liu, O. Teresaki, R. Ryoo, Nature 412 (2001) 169–172.
[27] A.B. Fuertes, D.M. Nevskaia, Microporous Mesoporous Mater. 62 (2003) 177–190.
[28] M. Kruk, M. Jaroniec, T.-W. Kim, R. Ryoo, Chem. Mater. 15 (2003) 2815–2823.
[29] A.-H. Lu, W. Schmidt, B. Spliethoff, F. Schüth, Adv. Mater. 15 (2003) 1602–1606.
[30] W.-H. Zhang, C. Liang, H. Sun, Z. Shen, Y. Guan, P. Ying, C. Li, Adv. Mater. 14 (2002) 1776–1778.
[31] A.-H. Lu, W. Li, W. Schmidt, W. Kiefer, F. Schüth, Carbon 42 (2004) 2939–2948.
[32] P. Michorczyk, J. Ogonowski, K. Zeńczak, J. Mol. Catal. 349 (2011) 1–12.
[33] M. Kruk, M. Jaroniec, Chem. Mater. 12 (2000) 1961–1968.
[34] R. Janus, M. Wądrzyk, P. Natkański, P. Cool, P. Kuśtrowski, J. Ind. Eng. Chem. 71 (2019) 465–480.
[35] M. Jaroniec, M. Kruk, J.P. Olivier, Langmuir 15 (1999) 5410–5413.
[36] A. Silvestre-Albero, J. Silvestre-Albero, M. Martínez-Escandell, R. Futamura, T. Itoh, K. Kaneko, F. Rodríguez-Reinoso, Carbon 66 (2014) 699–704.
[37] S.H. Joo, R. Ryoo, M. Kruk, M. Jaroniec, J. Phys. Chem. B 106 (2002) 4640–4646.
[38] R. Janus, P. Natkański, M. Wądrzyk, B. Dudek, M. Gajewska, P. Kuśtrowski, Mater. Today Commun. 13 (2017) 6–22.
[39] A. Silvestre-Albero, J. Silvestre-Albero, A. Sepúlveda-Escribano, F. Rodríguez-Reinoso, Microporous Mesoporous Mater. 120 (2009) 62–68.
[40] M.F.R. Pereira, J.J. M Órfão, J.L. Figueiredo, Appl. Catal. Gen. 184 (1999) 153–160.
[41] M.F.R. Pereira, J.L. Figueiredo, J.J. M Órfão, P. Serp, P. Kalck, Y. Kihn, Carbon 42 (2004) 2807–2813.
[42] M. Thommes, K. Kaneko, A.V. Neimark, J.P. Olivier, F. Rodríguez-Reinoso, J. Rouquerol, K.S.W. Sing, Pure Appl. Chem. 87 (9–10) (2015) 1051–1069.
[43] M. Thommes, Chem. Ing. Tech. 82 (7) (2010) 1059–1073.
[44] W. Schmitt, Microporous Mesoporous Mater. 117 (2009) 372–379.
[45] T. Onfroy, F. Guenneau, M.A. Springuel-Huet, A. Gédéon, Carbon 47 (2009), 2352–1357.
[46] F. Rodríguez-Reinoso, M. Molina-Sabio, Adv. Colloid Interface Sci. 76–77 (1998) 271–294.
[47] P. Serp, J.L. Figueiredo, Carbon Materials for Catalysis, John Wiley & Sons, New Jersey, 2009.
[48] R. Janus, A. Wach, P. Kuśtrowski, B. Dudek, M. Drozdek, A.M. Silvestre-Albero, F. Rodríguez-Reinoso, Langmuir 29 (2013) 3045–3053.
[49] P. Janus, R. Janus, P. Kuśtrowski, S. Jarczewski, A. Wach, A.M. Silvestre-Albero, F. Rodríguez-Reinoso, Catal. Today 235 (2014) 201–209.
[50] R. Janus, P. Natkański, A. Wach, M. Drozdek, Z. Piwowarska, P. Cool, P. Kuśtrowski, J. Therm. Anal. Calorim. 110 (2012) 119–125.
[51] F. Cavani, F. Trifiró, Appl. Catal. Gen. 133 (1995) 219–239.
[52] G. Emig, H. Hofmann, J. Catal. 84 (1983) 15–26.